Journal of Materials Science & Technology 57 (2020) 85–91

Contents lists available at ScienceDirect

Journal of Materials Science & Technology

journal homepage: www.jmst.org

Research Article

Probing deformation mechanisms of gradient nanostructured CrCoNi medium entropy alloy

Jia Li [a], Li Li [a], Chao Jiang [a], Qihong Fang [a,*], Feng Liu [b], Yong Liu [b], Peter K. Liaw [c]

[a] State Key Laboratory of Advanced Design and Manufacturing for Vehicle Body, Hunan University, Changsha, 410082, China
[b] State Key Laboratory of Powder Metallurgy, Central South University, Changsha, 410083, China
[c] Department of Materials Science and Engineering, The University of Tennessee, Knoxville, TN, 37996, USA

ARTICLE INFO

Article history:
Received 24 January 2020
Received in revised form 1 March 2020
Accepted 13 March 2020
Available online 3 June 2020

Keywords:
Medium entropy alloy
Gradient nanograined structure
Atomic simulation
Strengthening
Deformation
9R phase
Deformation twinning
Phase transformation

ABSTRACT

The gradient nanostructured medium entropy alloys (MEAs) exhibit a good yielding strength and great plasticity. Here, the mechanical properties, microstructure, and strain gradient in the gradient nanostructured MEA CrCoNi are studied by atomic simulations. The strong gradient stress and strain always occur in the deformed gradient nanograined MEA CrCoNi. The origin of improving strength is attributed to the formation of the 9R phase, deformation twinning, as well as the fcc to hcp phase transformation, which prevent strain localization. A microstructure-based predictive model reveals that the lattice distortion dependent solid-solution strengthening and grain-boundary strengthening dominate the yield strength, and the dislocation strengthening governs the strain hardening. The present result provides a fundamental understanding of the gradient nanograined structure and plastic deformation in the gradient nanograined MEA, which gives insights for the design of MEAs with higher strengths.

1. Introduction

High-entropy alloys (HEAs) have drawn great attention due to their excellent properties, such as high strength, outstanding thermal stability, as well as good resistances to wear, corrosion, and oxidation [1–6]. Recently, compared with the five-component CrMnFeCoNi HEA, an equiatomic medium-entropy alloy (MEA) CrCoNi shows the better mechanical properties, which are further enhanced at cryogenic temperatures [7–9]. The tensile strength of the MEA CrCoNi is almost 1 GPa at room temperature, and it improves to above 1.3 GPa at cryogenic temperatures due to the transition of deformation mechanism from the dislocation slip to deformation twinning [3,8].

However, HEAs and MEAs with coarse grains have a weakness in an excellent combination of strength and ductility. To overcome the strength-ductility trade-off in HEAs and MEAs, this issue could be solved through extensive strategies, such as grain-refinement strengthening [10], solid-solution strengthening [11], eutectic-structured strengthening [12], second-phase strengthening [13,14], twinning-induced plasticity (TWIP) [7,8], and transformation-induced plasticity (TRIP) strengthening [4], etc. Recently, a gradient hierarchical structure produced by cyclic dynamic torsion possesses a gradient distribution of grain sizes. It shows a dramatic enhancement in the tensile yielding strength and acceptable tensile ductility in Al0.1CoCrFeNi HEA [15]. More recently, the gradient nano-grained (GNG) structure generated by a machining method has been developed in the CrCoNi MEA, and leads to the great yield stress and high strain hardening [16]. However, the dynamical microstructural evolution (phase transformation, dislocation propagation, and deformation twinning) in the GNG MEA during the plastic deformation are extremely difficultly to be observed by experiments [17]. The molecular dynamics (MD) simulation, an atomic simulation method, is widely regarded as a supplement to the experimental techniques and theories [18], to grasp this deformed process of metals and alloys [19,20].

In spite of the intensive experimental investigation and atomic simulation, the corresponding theoretical work related to the strengthening of the GNG MEA is still lacking. Therefore, a microstructure-based predictive model should be proposed to quantitatively investigate the stress-strain response in the GNG MEA and HEA. A mechanism-based plasticity model has been developed to investigate the relationship between the microstructures and macroscopic mechanical properties of surface nanocrystallized materials [21]. However, no relevant model has been developed to

* Corresponding author.
E-mail address: fangqh1327@hnu.edu.cn (Q. Fang).

https://doi.org/10.1016/j.jmst.2020.03.064
1005-0302/

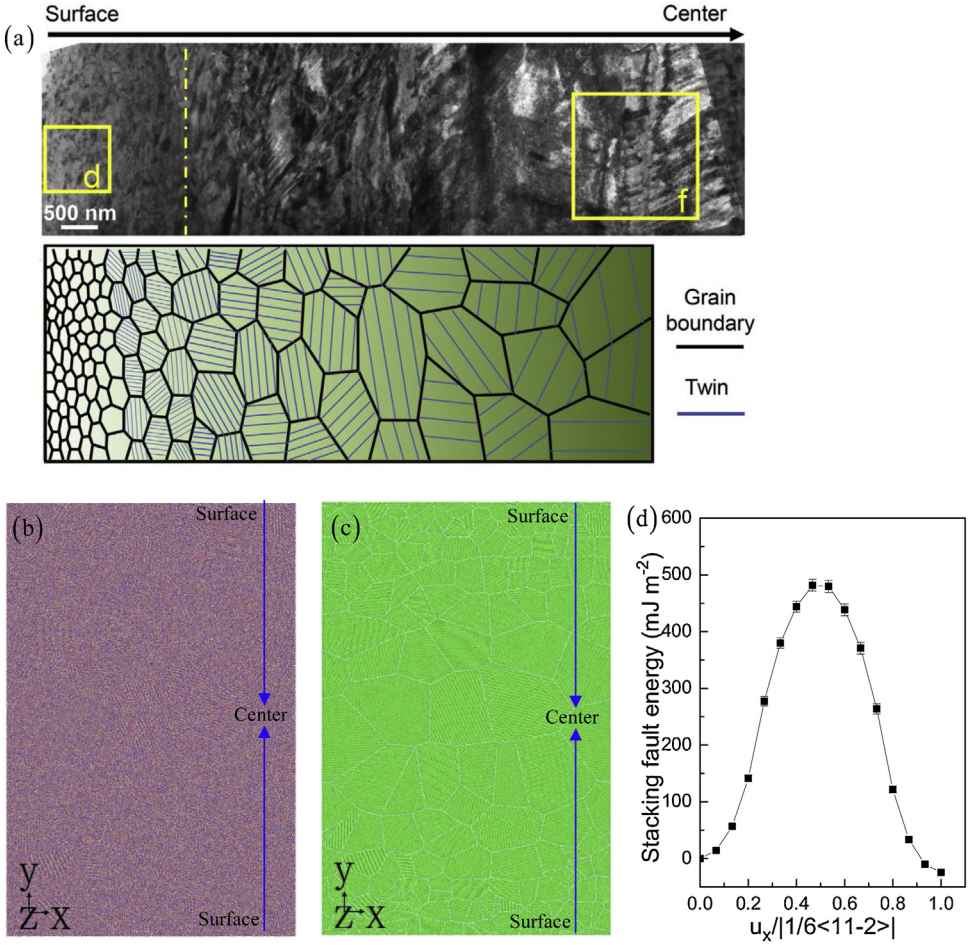

Fig. 1. TEM image revealing the gradient structure, and schematic image showing the gradient nanostructure after machining [16] (a). The atoms of the GNG MEA CrCoNi are colored based on the atomic type (b) and CNA value (c). Cr, Co, and Ni. Stacking fault energy vs. displacement (d).

describe the unique lattice distortion effect and other microstructural evolution on the mechanical behavior in the GNG MEA and HEA.

Here, we investigate the mechanical response and deformation mechanism of the GNG MEA during the tensile deformation using MD simulations. Furthermore, the underlying atomic-level deformation process can be directly observed, and a predictive microstructure-based constitutive model can be established, thereby shedding the light into the strengthening mechanisms of the GNG MEA.

2. MD simulation detail

Using MD simulations, the tensile deformation of the face-centered-cubic (fcc) GNG MEA CrCoNi prepared experimentally in Fig. 1(a) is presented in Fig. 1(b) and (c). Based on the previous experiment [7–9,16,22], the lattice parameter of the CrCoNi MEA is 3.524 Å. The GNG CrCoNi MEA shows the high yield strength [7–9]. In some nanocrystalline HEAs, the softening occurs when the grain size is less than 10–15 nm [23,24]. Here, the grain size of the GNG CrCoNi MEA increases gradually from 18.0 nm at the surface to 90.0 nm at the center, as shown in Fig. 1(c). The GNG MEA structure is constructed by the Voronoi method, and it has 190 grains with various orientations. The GNG MEA sample containing 99,734,808 atoms have the dimensions of 271.5 nm × 400.1 nm × 10.3 nm, where the thickness of the columnar grain is larger than the cutoff distance of 5 Å for meeting the periodicity along the z direction. The *z* direction is along the <110> direction, which allows the dislocation to glide on {112} slip systems [16,25]. To construct the desired GNG CrCoNi MEA sample, the atoms in the GNG Ni are randomly replaced by atoms of Cr and Co, as presented in Fig. 1(b).

Periodic boundary conditions are applying along *x* and *z* directions. The free boundary conditions are applying along y directions for meeting experimental results [16], which show the smallest grain of the GNG CrCoNi MEA adjacent to the free surface in Fig. 1(a). Here, the gradient nanostructured CrCoNi MEA film of three-dimensional (3D) columnar grains is built. To highlight the gradient grain effect on the deformation response, the sample width (the *y*-direction) is slightly larger than the sample length (the *x*-direction), which is similar to the previous report in the gradient nanostructured metals [15,16]. According to the Maxwell Boltzmann distribution, the velocities of all atoms are randomly set. The temperature of MD simulation is 300 K from experiments [16]. Prior to the loading, the sample is first subjected to the energy minimization using the conjugate gradient method, and NVT dynamics (the canonical ensemble with a constant number of particles, volume and temperature) at the temperature of 300 K for 100 ps in order to the relaxation. Then, NPT dynamics (the isothermal-isobaric ensemble with a constant number of particles, volume and pressure) at the temperature of 300 K is performed for 100 ps in order to the further relaxation. A time step is 1 fs. The uniaxial tensile loading with a constant strain rate of 1×10^8 s^{-1} is applied along *x*-direction under NPT dynamics at temperature of 300 K. The temperature in the NVT and NPT dynamics is adjusted by the Nose-Hoover method [19,20]. The maximum engineering strain reaches 10 %. A second nearest-neighbor modified embedded-atom

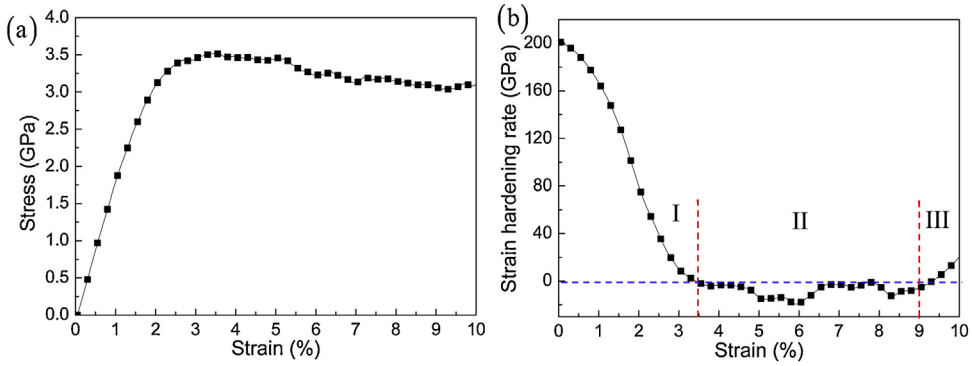

Fig. 2. Relationship between the stress and strain (a) and strain hardening rate as a function of strain (b).

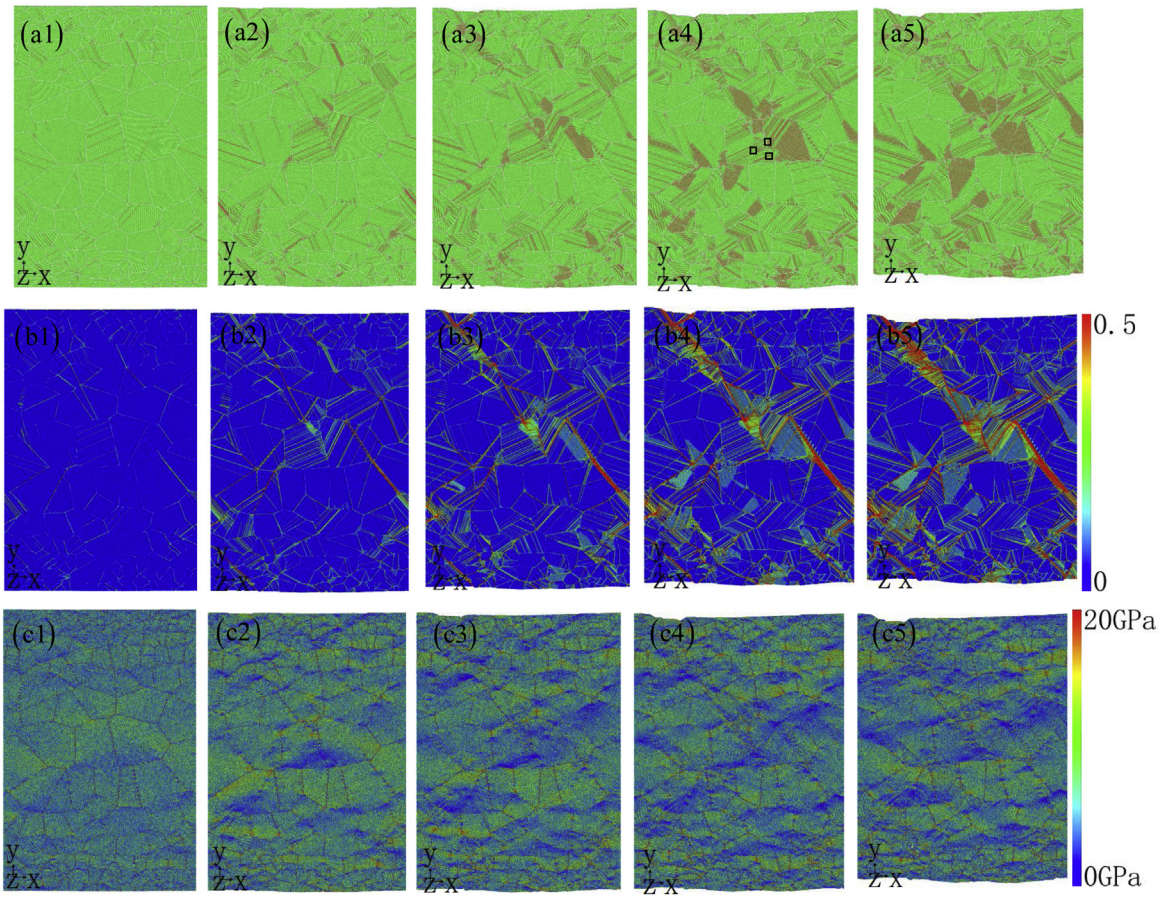

Fig. 3. Microstructures at different strains of 2% (a1), 4% (a2), 6% (a3), 8% (a4) and 10 % (a5). The distribution of strain (b1-b5) and stress (c1-c5) at different strains of 2%, 4%, 6%, 8%, and 10 %, respectively.

method (2 N N MEAM) potential [26] is employed to the interactions of atoms in the CrCoNi MEA. The current potential can clarify the fundamental reasons for sluggish diffusion and solid-solution hardening, and it is widely used in studying the mechanical properties during tensile/compressive deformation [27,28]. The MD simulations are computed by the open-source Large-scale Atomic/Molecular Massively Parallel Simulator code [29]. The local atomic structure is analyzed by the common-neighbor analysis (CNA), and the microstructural evolution is presented via the Ovito software [30]. Based on the value of CNA, the green color represents fcc structure, the red color stands for stacking fault structure, and the white color means other structure including dislocation, GB, and free surface in Fig. 1(c).

The deformation mechanism of nanocrystalline metal depends on the stacking fault energy (SFE), which determines deformation twinning or dislocation glide. Hence, the curve of the SFE in the CrCoNi MEA is presented in Fig. 1(d). Here, SFE for the fcc CrCoNi MEA is -24.5 ± 2.4 mJ m^{-2} in accordance with the previous work [7,16], leading to that the partial dislocations are more likely to occur, compared to the full dislocation.

3. Results and discussion

Here, the tension experiment is used to evaluate the effect of the observed structural change on the mechanical properties. Fig. 2 shows the stress and strain-hardening rate with the increase

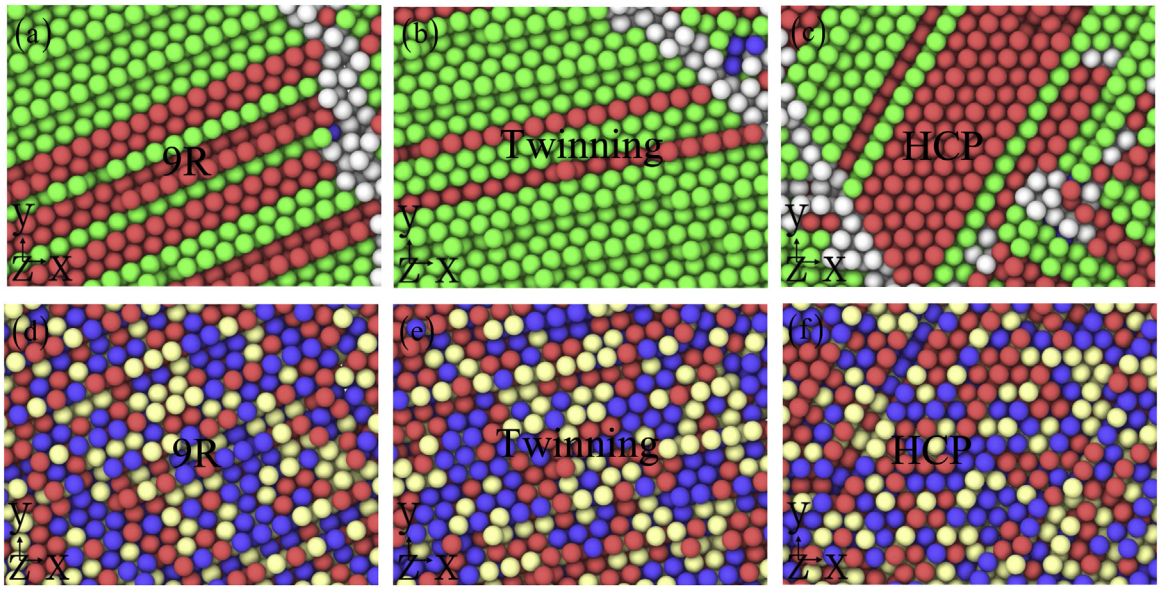

Fig. 4. The partially-enlarged view of 9R phase (a, d), deformation twinning (b, e), and hcp phase (c, f) at a strain of 8%. Atoms are colored according to the CNA (a-c), and according to the type (d-f). The corresponding regions are marked in Fig. 3(a4) by a black box.

of strain. The elastic modulus and yielding strength of the GNG CrCoNi MEA at 300 K are 179 GPa and 3.52 GPa. After yielding, the flow stress firstly decreases. At high strain, the flow stress declines sharply, and then its asymptotic behavior approaches a constant value. This transition takes place over a relatively narrow range of strain. As a main point of interest, Fig. 2(b) shows the strain hardening rate computed from the curve of Fig. 2(a). Based on Considere's criterion [31], a homogeneous deformation and a good ductility occur in a material with high strain-hardening capacity. The strain hardening rate reduces sharply up to the strain of 3.5 % at the stage "I", then keeps a value larger than −20 GPa at the stage "II", and finally increases gradually at the stage "III". The slope of the strain hardening rate curve in the second stage in strain ranges from 3.5 %–9.0 %, is almost zero, suggesting the sustained dislocation evolution during the deformation process.

In order to understand this strain hardening behavior, the dynamical microstructural evolution should be investigated completely to reveal the main deformation mechanisms. As a result, the partial dislocations are nucleated from grain boundaries (GBs), and then moved to the opposite GBs, producing the stacking faults left in the grain (see Fig. 3(a1-a5)). The current dislocation processes begin with small grains at the upper surface, and then gradually expand towards the large grains in the middle region. This conventional phenomenon is observed in a previous in situ TEM deformation experiment [31,32]. In addition, the contribution of GB sliding plays a key contribution to the plastic deformation of the GNG MEA. Analyses of the strains of GB atoms reveal larger strains located to neighbor GB than grain interiors. The GB sliding is consistent with the dependence of grain size [33]. Interestingly, a phase transition process from the fcc structure to 9R structure starts to be activated, as shown in Figs. 3(a3), 4 (a) and (d). The 9R structure sequence, ABCBCACAB, can be derived from the FCC structure by inserting an intrinsic stacking fault every third {111} plane, indicating that a low SFE is a key requirement for 9R structure. The 9R nucleus takes place from the triple grain junction in large grain of middle region, and the continuous migration of phase boundaries causes the growth of 9R phase. Ultimately, 9R phase across the whole grain forms (Fig. 3(a3-a5)), in agreement with the previous experimental observation [4,34]. Meanwhile, the deformation twinning and the fcc to hcp phase transformation occur in Figs. 3(a3-a5) and 4 (b–f), and then affect significantly the mechanical properties. Recently, a large number of experimental results further prove this view related to deformation twinning and phase transformation on the strength and ductility of HEA [35–38]. The strain-induced fcc to 9R phase transformation, the deformation twinning, and the fcc to hcp phase transformation, whose origin is related to the negative SFE to strongly affect the free energy difference between the fcc and hcp phases [39], play a major role in controlling the second stage of the strain hardening rate. Furthermore, when strain is larger than 8%, 9R phase and hcp phase are propagated along the GB from large to small grains, resulting in the slight increase of the stress (Fig. 2(a)).

To understand the trend of stress and strain distribution in the inside of the sample on the deformation mechanism of CrCoNi MEA, the evolutions of shear strain and stress along *x*-direction in the GNG CrCoNi at the different strains are shown in Fig. 3(b1-b5) and (c1-c5). With the increasing strain, the high local strain/stress concentration mainly appears in the middle region, and the low or free strain/stress region is located at the surface before the void nucleation (Fig. 3(b1)). The high strain exists GB, 9R phase, stacking fault, deformation twinning and hcp phase, to revel their contribution to plasticity. The shear band nucleation at the upper and lower surfaces results from a shear transformation zone [40], leading to the local necking of the GNG CrCoNi sample. The formation of shear band, deformation twinning, and phase transformation prevent strain localization (Fig. 3(b1-b5)), and then affect the plasticity of GNG CrCoNi. However, the stress distribution strongly changes from high to low values, even free, in the region where voids appeared (Fig. 3(c1-c5)). The phase transformation can release the local stress to the zero value, which would affect the plasticity [4,28,41].

4. Modeling

A microstructure-based theoretical model is proposed to quantitatively investigate the stress-strain response of GNG CrCoNi MEA in the present study. The mechanical behaviors of GNG CrCoNi MEA with grain sizes varying from several nanometers to tens of nanometers are established. In Fig. 5, the GNG CrCoNi MEA as the multi-phase composite structure is composed of *n* phases, which have various grain sizes. The dislocation-density-based model is

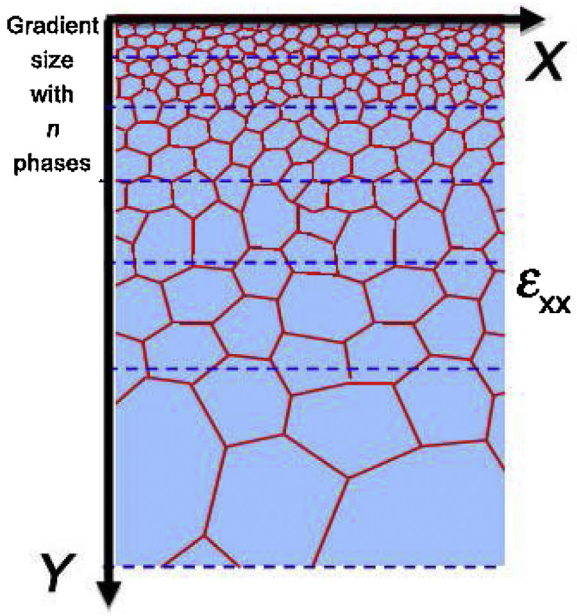

Fig. 5. Schematic of GNG CrCoNi MEA subjected to tensile strain of ε_{xx}, where GNG CrCoNi MEA is assumed as multi-phase composite structure of n phases with different grain sizes.

employed for modifications to predict the mechanical response of each phase in GNG CrCoNi MEA [42].

The total strain rate contains the elastic and plastic parts, respectively:

$$\dot{\varepsilon} = \dot{\varepsilon}^{e} + \dot{\varepsilon}^{p} \tag{1}$$

The elastic strain rate obtained from the Cauchy stress rate $\dot{\sigma}$, can be expressed as:

$$\dot{\varepsilon}^{e} = M : \dot{\sigma} \tag{2}$$

where M is the elastic compliance tensor of metals, and $\dot{\sigma}$ represents the stress tensor and a dot denotes differentiation with respect to time t. Based on the conventional J2-flow theory of plasticity, the plastic strain rate is proportional to the deviatoric stress σ' as:

$$\dot{\varepsilon}^{p} = \frac{3\dot{\varepsilon}^{p}}{2\sigma_{e}}\sigma' \tag{3}$$

where σ_e is the Mises equivalent stress. Here, $\sigma_e = \sqrt{3\sigma'_{ij}\sigma'_{ij}/2}$, and $\sigma'_{ij} = \sigma_{ij} - \sigma_{kk}\delta_{ij}/3$. $\dot{\varepsilon}^{p}$ is the equivalent plastic strain rate which is determined by:

$$\dot{\varepsilon}^{p} = \dot{\varepsilon}\left(\frac{\sigma_e}{\sigma_{flow}}\right)^{m_0} \tag{4}$$

where $\dot{\varepsilon} = \sqrt{2\dot{\varepsilon}'_{ij}\dot{\varepsilon}'_{ij}/3}$ denotes the equivalent strain rate and $\dot{\varepsilon}'_{ij} = \dot{\varepsilon}_{ij} - \dot{\varepsilon}_{kk}\delta_{ij}/3$. m_0 is the rate-sensitivity exponent, and usually takes a large value larger than 20. σ_{flow} is the flow stress. Despite the fact that the nanocrystalline material is strongly strain rate dependent [43–45], the strain rate dependence is not rigorously accounted for in the present constitutive model as the previous research [43,46]. Eqs. (2)–(4) establish the constitutive mechanism-based plasticity model for nanograined metals.

The flow stress of GNG CrCoNi MEA can be expressed as follows based on the individual contribution made by different strengthening mechanisms

$$\sigma_{flow} = \sigma_0 + M\alpha\mu b\sqrt{\rho} + \sigma_{GB} + \sigma_{ss} + \sigma_{twin} + \sigma_{9R} + \sigma_{hcp} \tag{5}$$

where σ_0 is the lattice friction stress. M, α, μ, b, and ρ are the Taylor factor, empirical constant, shear modulus, magnitude of Burgers vector, and dislocation density, respectively. σ_{GB} is GB strengthening, σ_{ss} denotes the lattice distortion dependent solid-solution strengthening, and σ_{twin} represents the twin boundary strengthening, σ_{9R} is the contributed stress from the 9R phase, σ_{hcp} derives from the fcc to hcp phase transition. On the basis of the Kocks-Mecking model [47–49], the dislocation density in the grain interior can be expressed as:

$$\frac{\partial\rho}{\partial\varepsilon^{p}} = M\left(\frac{1}{bd_G} + \frac{\psi\sqrt{\rho}}{b} - k_{20}\left(\frac{\dot{\varepsilon}^{p}}{\dot{\varepsilon}_0}\right)^{-1/m}\rho - k_e\rho\right) \tag{6}$$

where ψ is the proportionality factor, d_G is the grain size, k_{20} is the dynamic recovery constant, $\dot{\varepsilon}_0$ is the reference strain rate, m is inversely proportional to the temperature, and k_e is an additional dynamic recovery factor based on the previous work [43]. The first two terms on the right-hand side of the equation denote the athermal storage of dislocations, the third term represents the annihilation of dislocation during dynamic recovery which is independent of grain size, and the last term is accounted for the additional dislocation dynamic recovery at GBs introduced by nanoscale grains. k_e can be expressed as:

$$k_e = (d_e/d_G)^2 \tag{7}$$

where d_e denotes a critical grain size which represents the occurrence of reinforced dynamic recovery.

The GB strengthening, σ_{GB}, represents the contributed flow stress deriving from GB, which can be expressed as:

$$\sigma_{GB} = k_{HP}/d_G \tag{8}$$

where k_{HP} is the Hall-Petch constant of metals.

The solid-solution strengthening, σ_{ss}, denotes the contribution to the flow stress arising from the solutes in GNG CrCoNi MEA. According to the previous investigations [50,51], the expression of the solid-solution strengthening introduced by a single element in CrCoNi MEA can be expressed as:

$$\sigma_f^i = A\mu c_i^{2/3}\delta_i^{4/3} \tag{9}$$

where A is a non-dimensional constant dependent on the materials of the order of 0.04 [50], and c_i is the atomic fraction of individual principal elements in CrCoNi MEA. The mismatch parameter, δ_i, in Eq. (9) can be expressed as [52]:

$$\delta_i = \xi\left(\delta G_i^2 + \beta^2\delta r_i^2\right)^{1/2} \tag{10}$$

where ξ is equal to 1. It is generally believed that $3 < \beta < 16$ for screw dislocation, and $\beta > 16$ for edge dislocation [50,52]. Here, β is equal to 16 due to that the dominant dislocations are an edge type in the CrCoNi MEA. The elastic mismatch δG_i and the atomic size mismatch δr_i introduced by element i can be expressed as follows:

$$\delta r_i = \frac{\delta r_{ijk}^{ave} - \delta r_{jk}^{ave}}{\delta c_i} \tag{11}$$

$$\delta G_i = \frac{\delta G_{ijk}^{ave} - \delta G_{jk}^{ave}}{\delta c_i} \tag{12}$$

where δr_{ijk}^{ave} and δG_{ijk}^{ave} are the average atomic size mismatch and the average elastic mismatch of ijk MEA. δr_{jk}^{ave} and δG_{jk}^{ave} denote the average atomic size mismatch and the average elastic mismatch of jk binary alloy. δc_i represents the atomic fraction difference of

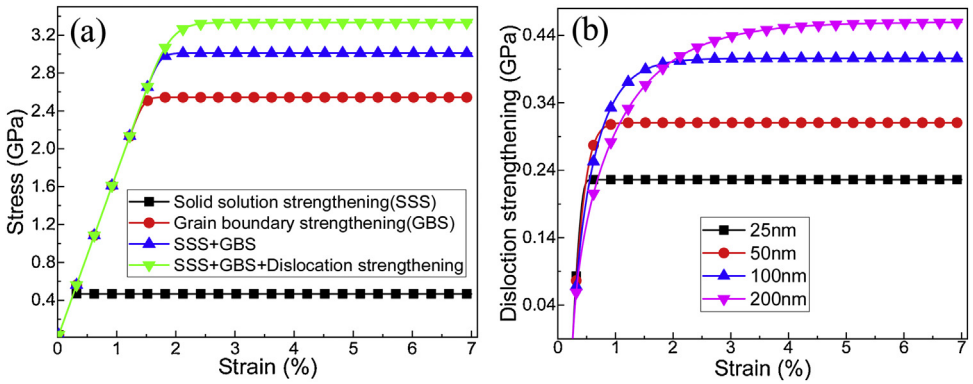

Fig. 6. The separate strengthening contributions in GNG CrCoNi MEA under deformation (a) and dislocation strengthening contribution of GNG CrCoNi MEA with different grain sizes (b).

the element i between the ijk MEA and jk binary alloy. The average elastic mismatch and atomic size mismatch can be expressed as

$$\delta r^{\text{ave}} = \sum_{i}^{n}\sum_{j}^{n} c_i c_j \delta r_{ij} = (c_1, c_2, \cdots, c_n) \begin{pmatrix} \delta r_{11} & \delta r_{12} & \cdots & \delta r_{1n} \\ \delta r_{21} & \delta r_{22} & \cdots & \delta r_{2n} \\ \vdots & \cdots & \ddots & \vdots \\ \delta r_{n1} & \delta r_{n2} & \cdots & \delta r_{nn} \end{pmatrix} \begin{pmatrix} c_1 \\ c_2 \\ \vdots \\ c_n \end{pmatrix} \quad (13)$$

$$\delta G^{\text{ave}} = \sum_{i}^{n}\sum_{j}^{n} c_i c_j \delta G_{ij} = (c_1, c_2, \cdots, c_n) \begin{pmatrix} \delta G_{11} & \delta G_{12} & \cdots & \delta G_{1n} \\ \delta G_{21} & \delta G_{22} & \cdots & \delta G_{2n} \\ \vdots & \cdots & \ddots & \vdots \\ \delta G_{n1} & \delta G_{n2} & \cdots & \delta G_{nn} \end{pmatrix} \begin{pmatrix} c_1 \\ c_2 \\ \vdots \\ c_n \end{pmatrix} \quad (14)$$

where δG_{ij} and δr_{ij} represent the elastic mismatch and the atomic size mismatch between the atoms i and j which can be written as [51]:

$$\delta r_{ij} = 2(r_i - r_j)/(r_i + r_j) \quad (15)$$

$$\delta G_{ij} = 2(G_i - G_j)/(G_i + G_j) \quad (16)$$

where r_i and r_j represent the atomic radii, G_i and G_j are the shear moduli of pure metal crystals i and j, respectively. Lastly, the solid-solution strengthening in MEA can be expressed as according to the Vegard's law [53]. Hence, the solid-solution strengthening in MEA can be written as

$$\sigma_{ss} = \sum c_i \sigma_{\text{f}}^{i} \quad (17)$$

where σ_{f}^{i} is calculated based on the Eq. (9).

The stress-strain response of a single phase in GNG CrCoNi MEA can be acquired based on Eqs. (1)–(17). The rule of mixtures of Voigt model is then employed to calculate the stress-strain response of the entire GNG CrCoNi MEA, in which an equal strain is assumed, as shown in the previous work [43,44,54]. As presented in Fig. 5, the tensile stress of GNG CrCoNi composed of n phases can be expressed as:

$$\sigma_{\text{xx}} = \frac{\Sigma_{i=1}^{n} \sigma_{\text{xx}i} h_i}{h} \quad (18)$$

where i and n represent the ith phase and the number of phases in GNG region, respectively. $\sigma_{\text{xx}i}$ is the stress applied on the phase i, $h_i = h/n$ is the thickness of n phase, and h denotes the thickness of the whole GNG CrCoNi MEA. All the parameters used in the present model are listed in Table 1.

Fig. 6(a) compares the contribution from different strengthening mechanisms in GNG CrCoNi MEA. The lattice distortion dependent solid-solution strengthening and GB strengthening mainly contribute to the yield strength, while the dislocation evolution in grain interior mainly enhances the strain hardening. Thereinto, GB strengthening contributes the most to the increase of yield stress owing to fine grain size. The solid-solution strengthening is not significant compared to GB strengthening in the GNG MEA. The summing stress derived from the solid-solution strengthening and GB strengthening is about 3.04 GPa. The total yield stress is larger than 3.04 GPa, the remaining stress maybe contributed from the twin boundary strengthening, strain-induced 9R phase, and fcc to hcp phase transformation. However, there is no reasonable model considering the strengthening contribution from 9R phase [55]. Based on the previous study, the twin boundary contributed stress can be expressed as $k_{\text{TB}}\lambda^{-0.5}$, λ represents the average twin thickness. It is supposed that k_{TB} is equal to the Hall-Petch constant, which is the same as that in the previous study. The MD simulation results indicate that the total volume fraction of twin boundaries, 9R phase, and hcp phase are about 5 %–10 %. Therefore, the predicted results are consistent with the MD simulation results. The dislocation in the grain interior only provides strain hardening during the initial stage of plastic deformation owing to consideration of additional dislocation dynamic recovery at GBs introduced by nanoscale grains. Fig. 6(b) shows the strain hardening stress derived from the dislocation strengthening for different grain sizes. The results show that dislocation strengthening decreases with the increasing grain sizes. This trend indicates nanocrystalline material lacks strain hardening capability. Moreover, the strain for the dislocation strengthening reaching the maximum stress increases with increasing the grain sizes. This result is due to the fact that the increasing grain size increase the dislocation storage capacity, which could improve the ductility of the materials.

Table 1
Material parameters used in the present model for the GNG CrCoNi MEA.

Parameter	Symbol	Magnitude
Elastic modulus (GPa)	E	179
Shear modulus (GPa)	μ	68.8
Poisson's ratio	ν	0.3
Magnitude of the Burger vector (nm)	b	0.256
Empirical constant	α	0.33
Taylor factor	M	3.06
Dynamic recovery constant	k_{20}	21.6
Proportionality factor	ψ	0.025
Dynamic recovery constant	m	21.5
Reference strain rate (s^{-1})	$\dot{\varepsilon}_0$	1
Hall–Petch slope (MP $m^{1/2}$)	k_{HP}	0.8
Reference grain size (nm)	d_{e}	580

5. Conclusion

In the present work, mechanical properties of the GNG CrCoNi MEA are studied, and the microstructure after tension is examined over a wide range of strain. It is found that the flow stress firstly decreases steadily, and then maintains stability with the increasing strain after yielding. The origin of the high strength in the GNG structure is attributed to the stronger gradient strain and stress. The phase transformation, 9R phase, and deformation twinning observed in large grains can prevent the strain localization, resulting in improving the strength. It has been found that GB strengthening dominates the yield strength, and the dislocation in the grain interior promotes the strain hardening. In addition, the dislocation in the grain interior only contributes strain hardening at the initial stage of the plastic deformation based on the proposed model. This finding gives a new meaning to activate the dislocation synergistic phase transformation, for tuning microstructures to obtain the superior properties of advanced GNG MEAs.

Declaration of Competing Interest

No potential conflict of interest was reported by the authors.

Acknowledgements

This work was supported financially by the Foundation for Innovative Research Groups of the National Natural Science Foundation of China (No. 51621004), the National Natural Science Foundation of China (Nos. 51871092, 11772122 and 51771233), the State Key Laboratory of Advanced Design and Manufacturing for Vehicle Body (No. 71865015), the National Key Research and Development Program of China (Nos. 2016YFB0700300 and 2016YFB1100103) and the Hunan Provincial Innovation Foundation For Postgraduate (No. CX2018B156). The authors gratefully acknowledge Dr. Zhi Zeng for his gradient nanostructured model set-up. Peter K. Liaw very much appreciates the support of the U.S. Army Research Office Project (Nos. W911NF-13-1-0438 and W911NF-19-2-0049) with the program managers, Drs. M.P. Bakas, S.N. Mathaudhu, and D.M. Stepp. Peter K. Liaw thanks the support from the National Science Foundation (Nos. DMR-1611180 and 1809640) with the program directors, Drs. J. Yang, J.G. Shiflet and D. Farkas.

References

[1] J.W. Yeh, S.K. Chen, S.J. Lin, J.Y. Gan, T.S. Chin, T.T. Shun, C.H. Tsau, S.Y. Chang, Adv. Eng. Mater. 6 (2004) 299–303.
[2] Y. Zhang, T.T. Zuo, Z. Tang, M.C. Gao, K.A. Dahmen, P.K. Liaw, Z.P. Lu, Prog. Mater. Sci. 61 (2014) 1–93.
[3] B. Gludovatz, A. Hohenwarter, D. Catoor, E.H. Chang, E.P. George, R.O. Ritchie, Science 345 (2014) 1153–1158.
[4] Z. Li, K.G. Pradeep, Y. Deng, D. Raabe, C.C. Tasan, Nature 534 (2016) 227–230.
[5] O. El-Atwani, N. Li, M. Li, A. Devaraj, J.K.S. Baldwin, M.M. Schneider, E. Martinez, Sci. Adv. 5 (2019) 2002.
[6] Z.F. Lei, X.J. Liu, Y. Wu, H. Wang, S.H. Jiang, S.D. Wang, X.D. Hui, Y.D. Wu, B. Gault, P. Kontis, D. Raabe, L. Gu, Q.H. Zhang, H.W. Chen, H.T. Wang, J.B. Liu, K. An, Q.S. Zeng, T.G. Nieh, Z.P. Lu, Nature 563 (2018) 546–550.
[7] Z. Zhang, H. Sheng, Z. Wang, B. Gludovatz, Z. Zhang, E.P. George, R.O. Ritchie, Nat. Commun. 8 (2017) 14390.
[8] B. Gludovatz, A. Hohenwarter, K.V. Thurston, H. Bei, Z. Wu, E.P. George, R.O. Ritchie, Nat. Commun. 7 (2016) 10602.
[9] Y. Ma, F. Yuan, M. Yang, P. Jiang, E. Ma, X. Wu, Acta Mater. 148 (2018) 407–418.
[10] F. Otto, A. Dlouhý, C. Somsen, H. Bei, G. Eggeler, E.P. George, Acta Mater. 61 (2013) 5743–5755.
[11] Z.W. Wang, I. Baker, Z. Cai, S. Chen, J. Poplawsky, W. Guo, Acta Mater. 120 (2016) 228–239.
[12] Y. Lu, Y. Dong, S. Guo, L. Jiang, H. Kang, T. Wang, B. Wen, Z. Wang, J. Jie, Z. Cao, H. Ruan, T. Li, Sci. Rep. 4 (2014) 6200.
[13] L. Rogal, D. Kalita, A. Tarasek, P. Bobrowski, F. Czerwinski, J. Alloys. Compd. 708 (2017) 344–352.
[14] Y. Zhao, T. Yang, J. Zhu, D. Chen, Y. Yang, A. Hu, C. Liu, J. Kai, Scr. Mater. 148 (2018) 51–55.
[15] G. Chen, J. Qiao, Z. Jiao, D. Zhao, T. Zhang, S. Ma, Z. Wang, Scr. Mater. 167 (2019) 95–100.
[16] W. Guo, Z. Pei, X. Sang, J. Poplawsky, S. Bruschi, H. Bei, Acta Mater. 170 (2019) 176–186.
[17] F. Kacher, T. Zhu, O. Pierron, D.E. Spearot, Curr. Opin. Solid State Mater. Sci. 23 (2019) 117–128.
[18] E. Ma, T. Zhu, Mater. Today 20 (2017) 323–331.
[19] L.A. Zepeda-Ruiz, A. Stukowski, T. Oppelstrup, V.V. Bulatov, Nature 550 (2017) 492–495.
[20] X. Ke, J. Ye, Z. Pan, J. Geng, M.F. Besser, D. Qu, A. Caro, D. Qu, F. Sansoz, Nat. Mater. 18 (2019) 1207–1214.
[21] J. Li, A.K. Soh, Int. J. Plast. 39 (2012) 88–102.
[22] Q. Ding, X. Fu, D. Chen, H. Bei, B. Gludovatz, J. Li, Z. Zhang, E.P. George, Q. Yu, T. Zhu, R.O. Ritchie, Mater. Today 25 (2019) 21–27.
[23] J.L. Hou, Q. Li, C.B. Wu, L.M. Zheng, Materials 12 (2019) 1010.
[24] S. Chen, Z.H. Aitken, Z. Wu, R. Banerjee, Y. Zhang,Mater. Sci. Eng. A 773 (2020), 138873.
[25] X. Liu, H. Yin, Y. Xu, Materials 10 (2017) 1312.
[26] W.M. Choi, Y.H. Jo, S.S. Sohn, S. Lee, B.J. Lee, NPJ Comput. Mater. 4 (2018) 1.
[27] Q. Fang, Y. Chen, J. Li, C. Jiang, B. Liu, Y. Liu, P.K. Liaw, Int. J. Plast. 114 (2019) 161–173.
[28] J. Li, H. Chen, S. Li, Q. Fang, Y. Liu, L. Liang, Mater. Sci. Eng. A 760 (2019) 359–365.
[29] S. Plimpton, J. Comput. Phys. 117 (1995) 1–19.
[30] A. Stukowski,Model. Simul. Mater. Sci. Eng. 18 (2009), 015012.
[31] T.H. Courtney, Mechanical Behavior of Materials, Waveland Press, 2005.
[32] J. Kacher, B. Eftink, B. Cui, I. Robertson, Curr. Opin. Solid State Mater. Sci. 18 (2014) 227–243.
[33] N.Q. Vo, R.S. Averback, P. Bellon, S. Odunuga, A. Caro,Phys. Rev. B 77 (2008), 134108.
[34] W. Wu, B. Wei, S. Ni, Y. Liu, M. Song, Intermetallics 96 (2018) 104–110.
[35] F. Otto, A. Dlouhý, C. Somsen, H. Bei, G. Eggeler, E.P. George, Acta Mater. 61 (2013) 5743–5755.
[36] S. Chen, H. Oh, B. Gludovatz, S.J. Kim, E.S. Park, Z. Zhang, Q. Yu, Nat. Commun. 11 (2020) 1–8.
[37] H.Y. Diao, R. Feng, K.A. Dahmen, P.K. Liaw, Curr. Opin. Solid State Mater. Sci. 21 (2017) 252–266.
[38] H. Huang, Y. Wu, J. He, H. Wang, X. Liu, K. An, Z. Lu,Adv. Mater. 29 (2017), 1701678.
[39] Y. Koizumi, S. Suzuki, K. Yamanaka, B. Lee, K. Sato, Y. Li, S. Kurosu, H. Matsumoto, A. Chiba, Acta Mater. 61 (2013) 1648–1661.
[40] K. Albe, Y. Ritter, D. Sopu, Mech. Mater. 67 (2013) 94–103.
[41] J. Li, Q. Fang, B. Liu, Y. Liu, Acta Mater. 147 (2018) 35–41.
[42] Y. Estrin, H. Mecking, Acta Metall. 32 (1984) 57–70.
[43] J. Li, W. Lu, S. Chen, C. Liu,Int. J. Plast. 126 (2020), 102626.
[44] H. Jin, J. Zhou, Y. Chen, Mater. Sci. Eng. A 725 (2018) 1–7.
[45] M. Dao, L. Lu, R. Asaro, J. De Hosson, E. Ma, Acta Mater. 55 (2007) 4041–4065.
[46] L. Zhu, H. Ruan, X. Li, M. Dao, H. Gao, J. Lu, Acta Mater. 59 (2011) 5544–5557.
[47] H. Mecking, U. Kocks, Acta Metall. 29 (1981) 1865–1875.
[48] L. Capolungo, C. Jochum, M. Cherkaoui, J. Qu, Int. J. Plast. 21 (2005) 67–82.
[49] L. Capolungo, M. Cherkaoui, J. Qu, Int. J. Plast. 23 (2007) 561–591.
[50] C. Lee, G. Song, M.C. Gao, R. Feng, P. Chen, J. Brechtl, Y. Chen, K. An, W. Guo, J.D. Poplawsky, S. Li, A.T. Samaei, W. Chen, A. Hu, H. Choo, P.K. Liaw, Acta Mater. 160 (2018) 158–172.
[51] O.N. Senkov, J.M. Scott, S.V. Senkova, D.B. Miracle, C.F. Woodward, J. Alloys. Compd. 509 (2011) 6043–6048.
[52] R. Labusch, Phys. Status Solidi A 41 (1970) 659–669.
[53] A.R. Denton, N.W. Ashcroft, Phys. Rev. A 43 (1991) 3161–3164.
[54] T.W. Clyne, P.J. Withers, An Introduction to Metal Matrix Composites, Cambridge University Press, Cambridge, 1995.
[55] J.D. Zuo, C. He, M. Cheng, K. Wu, Y.Q. Wang, J.Y. Zhang, G. Liu, J. Sun, Acta Mater. 174 (2019) 279–288.